Lawrence Berkeley National Laboratory

Title

A 5-μm pitch charge-coupled device optimized for resonant inelastic soft X-ray scattering

Permalink

Journal

ISSN

Authors

Andresen, NC
Denes, P
Goldschmidt, A
et al.

Publication Date

DOI

A 5-µm pitch charge-coupled device optimized for resonant inelastic soft X-ray scattering

N. C. Andresen, P. Denes, A. Goldschmidt, J. Joseph, A. Karcher, and C. S. Tindall

A 5-*µm* pitch charge-coupled device optimized for resonant inelastic soft X-ray scattering

N. C. Andresen, P. Denes, A. Goldschmidt,[a)] J. Joseph, A. Karcher, and C. S. Tindall
Lawrence Berkeley National Laboratory (LBNL), 1 Cyclotron Road, Berkeley, California 94720, USA

We have developed a charge-coupled device (CCD) with 5 *µm* × 45 *µm* pixels on high-resistivity silicon. The fully depleted 200 *µm*-thick silicon detector is back-illuminated through a 10 nm-thick *in situ* doped polysilicon window and is thus highly efficient for soft through >8 keV hard X-rays. The device described here is a 1.5 megapixel CCD with 2496 × 620 pixels. The pixel and camera geometry was optimized for Resonant Inelastic X-ray Scattering (RIXS) and is particularly advantageous for spectrometers with limited arm lengths. In this article, we describe the device architecture, construction and operation, and its performance during tests at the Advance Light Source (ALS) 8.0.1 RIXS beamline. The improved spectroscopic performance, when compared with a current standard commercial camera, is demonstrated with a ~280 eV (C$_K$) X-ray beam on a graphite sample. Readout noise is typically 3-6 electrons and the point spread function for soft C$_K$ X-rays in the 5 *µm* direction is 4.0 *µm* ± 0.2 *µm*. The measured quantum efficiency of the CCD is greater than 75% in the range from 200 eV to 1 keV. © *2017 Author(s). All article content, except where otherwise noted, is licensed under a Creative Commons Attribution (CC BY) license (http://creativecommons.org/licenses/by/4.0/).* [http://dx.doi.org/10.1063/1.4997727]

I. INTRODUCTION

In 1D Resonant Inelastic X-ray Scattering (RIXS), a sample is illuminated with a monochromatic beam of X-rays, and a single electronic transition of a specific element is excited. In the resonant process the atom decays back to the ground state emitting an X-ray of very similar energy. The slight loss of energy provides information on the intrinsic excitations of the molecule/material in which the atom is embedded. The process, which with soft X-rays can probe the sample bulk to depths of 0.1 *µm* or more, can provide intrinsically sharp spectra because the final state is the atom in its ground state.[1]

In a RIXS experiment, the scattered (outgoing) X-rays are measured in a spectrometer that focuses the X-rays onto a grating, which, in turn, disperses them according to their energies. The angular-dispersion is converted to a position-dispersion in a (preferably long) flight path within the spectrometer arm. At the focal plane, an X-ray camera captures the spectrum image. Here, the energy dispersion is in one dimension and thus the spectral features are approximately straight lines in the other dimension. The resolving power—the ability to distinguish two close spectral lines—of the spectrometer is determined primarily by the spectrometer arm length, the X-ray optics quality and the X-ray camera position resolution in the dispersion direction.

The best currently used commercially available X-ray cameras have, at present time, 13.5 × 13.5 and 16 × 16 *µm* pixels.[2,3] They typically obtain resolutions of 10 *µm* RMS in the soft X-ray region.[4] Of these, the newer electron multiplying CCD cameras can achieve, depending on the setup, significantly better resolution[5] through the use of centroiding algorithms, albeit at the expense of dynamic range and/or limits on the maximum occupancy (rate).

In this article, we report on the development, construction, and operation of a new charge-coupled device (CCD) with 5 *µm* × 45 *µm* pixels with the goal to improve the RIXS spectrometry resolving power. The critical 5 *µm* dimension is intended to be deployed parallel to the energy dispersion direction of the spectrometer. The CCD was designed at Lawrence Berkeley National Laboratory (LBNL), and wafers are commercially fabricated by Teledyne DALSA semiconductor. The 2.5 *µm* Teledyne DALSA CCD process has a typical minimum pixel size of 10.5 *µm*. To overcome this size limitation, we designed a CCD that shifts charges in opposite vertical directions for adjacent columns, thus reducing the linear density of pixels in the horizontal (shift) register by a factor of two. In addition, the new CCD does not utilize channel-stops (commonly used in standard CCDs to avoid charge spilling onto neighbor columns) to further reduce the inter-column distance. Besides these two features, most other aspects of the design are based on CCDs on high-resistivity *n*-type silicon with thin entrance windows for extended blue and red sensitivity developed for supernova cosmology[6] at LBNL. We have also developed X-ray sensitive CCDs for fast, 2D soft X-ray detection.[7]

This article is organized in the following manner: Sec. II describes the CCD architecture and represents the core advancement. Section III describes the X-ray camera system including mechanical and readout components. Section IV presents the tests that were performed both on the bench and at dedicated tests at X-ray beam lines. In Sec. V, we discuss plans and ideas for further development of this device.

---

a)Author to whom correspondence should be addressed: agoldschmidt@lbl.gov

88, 083103-1

II. CCD ARCHITECTURE

X-rays enter the device through a thin and conductive back window. In order to maximize detection efficiency at C_K, window thicknesses of ~10 nm are required. The conductive window is held at a positive voltage sufficient to deplete the bulk. X-rays photoconvert in the bulk of the n-type high resistivity silicon, creating electron/hole pairs. The holes are then collected in a buried p-channel implant on the front side of the CCD, which is the region with the most negative voltage. The device functions as a conventional 3-phase MOS CCD, where the accumulated charge in the image area is then shifted row-by-row by clocking the voltages on the polysilicon gates. Unlike a conventional CCD, the polysilicon gates are laid out in such a way that adjacent columns have mirrored phases: as a result, charge moves in odd columns in opposite direction to the even columns.

At the end of the column, the charges of a row of pixels are transferred to the horizontal (shift) registers, one above and one below, where a separate set of three phase clocks move the charge to the four corners of the device for readout. Figure 1 shows a schematic view of the CCD with the pixel

FIG. 2. CCD device (front side in view) wire-bonded to a flexible circuit and mechanically supported by a silicon carbide (SiC) to which is also thermally coupled. X-rays enter through a cut-out in the SiC to the back side of the device (not shown). Note that in this image the CCD columns run horizontally.

and gate geometry and the path that holes make through the p-channel.

The 200 μm thickness was chosen to allow device post-processing at the wafer level. Soft X-rays, e.g., C_K, convert very near to the entrance window, so that the collected holes must travel through all 200 μm of silicon. As the substrate is fully depleted, charge is collected by drift rather than diffusion; however, scattering degrades the spatial resolution. As discussed below, future devices will be produced on thinner substrates.

A. Fabrication

The thin 10 nm, *in situ* doped polysilicon (ISDP), window must be processed after the front-end CCD processing has taken place. Wafers are produced by Teledyne DALSA semiconductor in their 2.5 μm CCD process. Wafers are then thinned, and the ISDP window is deposited using a chemical vapor deposition (CVD) process at the MicroSystems Laboratory (MSL) at LBNL. The CVD process requires temperatures above the aluminum melting point. Therefore, in the last step, one layer of metal and contacts are deposited lithographically in the MSL facilities.

The wafer is then diced and the individual CCD chips are glued to the supporting SiC along with the flex circuit to which, then, is wire-bonded. Figure 2 shows the finished CCD on its SiC/flex support.

III. CAMERA SYSTEM

A. Mechanical support, dewar, and temperature control

Leakage current from the 200 μm-thick volume of the CCD is prohibitively large at room temperature. Operation temperatures below approximately −100 °C are required to
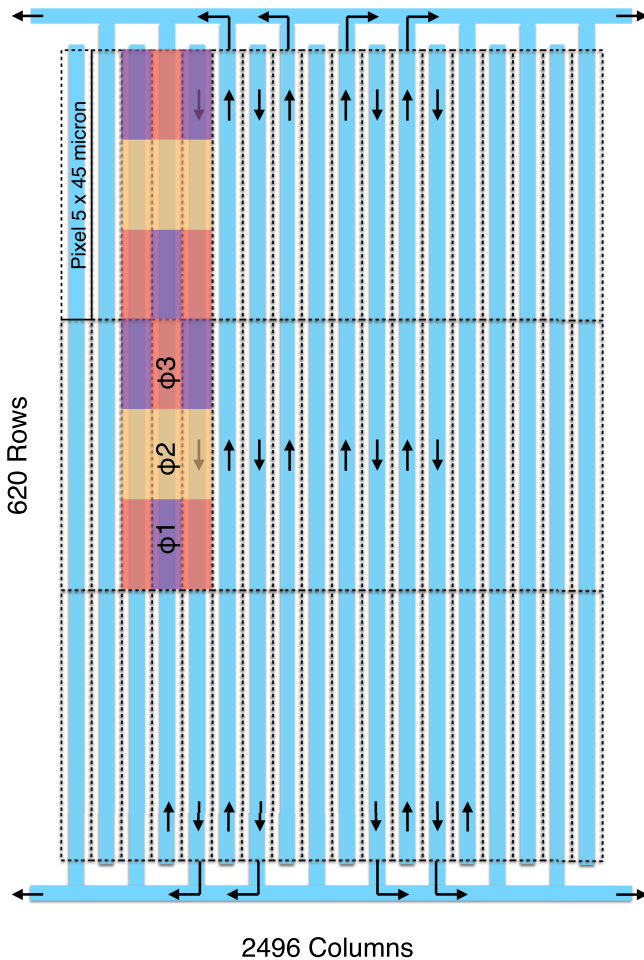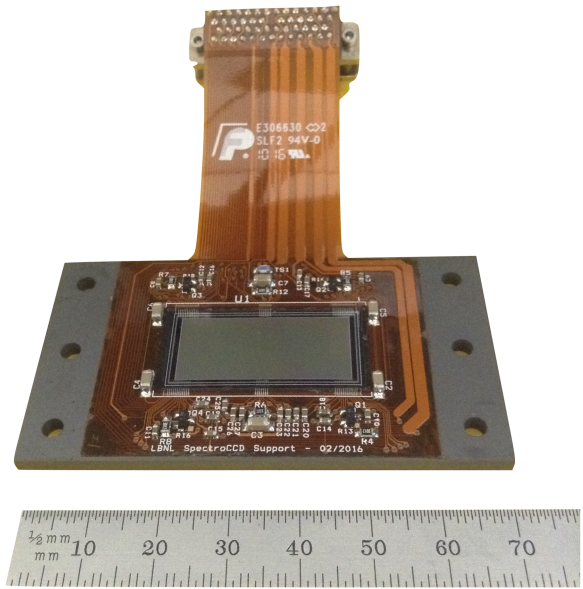

FIG. 1. CCD architecture. Holes accumulate in and travel through the buried p-channels (in light blue). The polysilicon gate structure provides 3-clock phases ($\varphi 1$, $\varphi 2$, and $\varphi 3$ shown in colors over six of the pixels) that shift charges along the column in opposite directions for adjacent columns. At the four corners, the pixels' charges are measured and sub-sequentially discarded. No channel stops are used in order to reduce the pixel width to the minimum.

prevent leakage current fluctuations from setting the noise floor during long (minutes-hours) exposures. To that end, the CCD is thermally coupled to a liquid nitrogen (LN_2) volume within a dewar and operated in vacuum. The dewar is a custom-designed double-walled stainless steel cylindrical container of approximately 10 cm diameter by 18 cm length with: an opening to introduce LN_2, vacuum electrical feedthroughs for CCD and temperature control and readout, and a 6-in. diameter conflat flange to attach the camera to a beam line. The SiC CCD support is bolted to a stainless-steel frame with which is thermally coupled but from which is electrically isolated. Four 3 cm-long metal rods support the stainless-steel frame and provide thermal contact to the LN_2 container wall.

For temperature control by means of an external Lakeshore 325 device, a resistance temperature detector (RTD) is attached to the stainless-steel frame as well as two heating resistors. The typical base temperature with the CCD in operation is -120 to -130 °C. A LN_2 fill lasts for more than 6 h without requiring refilling.

B. Readout system

1. CCD output stage

Charge from a pixel is shifted through the horizontal register until it reaches the gate on an on-chip pMOSFET output source-follower transistor. The capacitance at that node converts the charge into a voltage, which is, in turn, buffered by the source follower. In the flex circuitry, the voltage signal is further buffered by an external JFET and is capacitively coupled to the rest of the readout electronics outside the dewar where it is further amplified and digitized (see section below). Prior to depositing pixel charge on the output node, the node is cleared by means of a reset pMOSFET transistor. To reduce noise, correlated double sampling is performed by subtracting the signal voltage from the reset voltage.

2. CCD controller

The CCD controller supplies the bias voltage needed to deplete the CCD, the clocks and supply voltages for the output and reset transistors. The controller orchestrates the timing sequence to go from an exposure, through the transfer of the pixels' charges to the readout, to digitization and finally assembly of a digital image.

It consists of four custom electronic boards: a motherboard, a clock board, a power board, and a video board. The motherboard provides connectivity with the other three boards and with an Enclustra MARS MX2 board with a Xilinx Spartan 6 FPGA that supports a soft processor. A stripped-down Linux operating system runs on the soft ARM core and is accessible through the Ethernet network.

The clock board has 40 16-bit DAC channels to produce 20 clock outputs (each with a high and low setting) that are each amplified and buffered with an output from -15 V to 15 V. The high/low selection is done directly by the system FPGA. A peripheral interface controller (PIC) sets the DAC values, digitizes the clock analog outputs for monitoring, and actuates individual switches at the clock analog outputs.

Similarly, the video board has 20 16-bit DAC channels to control the high and low voltage states required for operation of the output and reset resistors of the 4 CCD analog outputs. These single ended outputs are then scaled in programmable gain amplifiers (PGA), converted to differential signals and digitized in a 4-channel 16-bit ADC at 100 mega-samples per second. The digitized data for the four output channels are transmitted to the FPGA via 8 low voltage differential signals (LVDS).

Last, the power board uses the externally supplied +24 V source to produce heavily filtered 3.3 V, 5.0 V, ±15.0 V, and ±30.0 V for use by the other boards.

3. Data acquisition system and image processing

The CCD controller runs a web server that provides the main control and monitor access point to operate the CCD from any web browser program in a computer in the same Ethernet network. All DAC voltages are set through web pages. A timing file, which is uploaded to the controller through one of the web pages, provides the real-time sequence with single-clock (10 ns) granularity for the various operations or modes: (1) exposure, charge transfer, and readout; (2) clear image; and (3) idle (clocking-out the CCD charge continuously but not assembling an image). The timing sequence is written with a custom low-level language with a small instruction set. Some parameters for the timing sequence (e.g., the number of clock cycles per vertical clock phase or the number of rows and columns to read out) can also be provided via the HTML/web graphical user interface. Upon the acquisition of a CCD image by the controller FPGA, the image data are stored in a FITS[8] file format and can then be downloaded via a controller web page.

Once downloaded, the image is processed using an ImageJ[9] script that (1) subtracts a background image, (2) removes vertical and horizontal over-scan regions (rows and columns that are read out but do not correspond to physical image-area pixels), (3) equalizes the charge-to-ADC gain in the four readout quadrants, and, last, (4) reassembles the image by interleaving the columns from the top and bottom quadrants.

In continuous data taking mode, an ImageJ script spawns a Python process that interacts with the controller through the HTML pages to produce and download an image, which is then processed and displayed by the ImageJ script.

IV. CAMERA PERFORMANCE

A. Characterization with ^{55}Fe source

Laboratory characterization was performed with a sealed ^{55}Fe X-ray source (5.9 keV X-rays). The source is located outside of the vacuum dewar and a thin window made from layers of thin aluminized Mylar and Kapton is used as a vacuum window and ambient light block. Typical exposures of a few-seconds duration yielded images with hundreds of X-ray interactions each.

Recorded images are background subtracted and gain corrected. Figure 3 shows a zoom of a small region of a CCD image with ^{55}Fe X-ray hits. A local-maxima finding algorithm
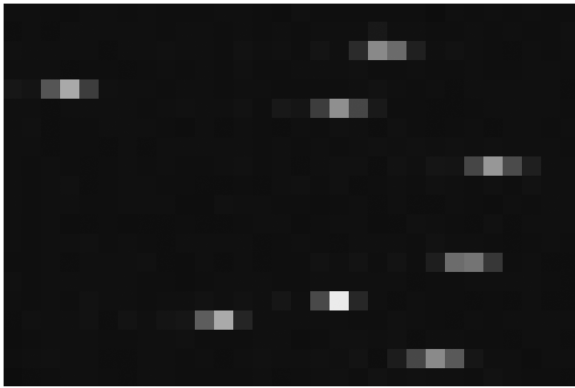
FIG. 3. 30 × 20 pixel area of a CCD image with 5.9 keV ^{55}Fe X-rays. The pixels—shown here as squares—are actually 45 μm in the vertical direction and 5 μm in the horizontal. The lowest pixel ADC value is black and the maximum is white.

is used to clusterize the X-ray hits. An integration of pixel values around the local maxima renders a charge spectrum in raw ADC counts, as shown in Fig. 4. As 5.9 keV X-rays in silicon produce on average 1620 electron-hole pairs, from the charge distribution peak we obtain the overall system gain conversion factor: 0.48 ADU per hole.

The pixel charge noise is obtained from a distribution of pixel ADC values in images without X-ray exposure (or from the vertical over-scan region). To achieve low noise levels, the signal voltage from the charge in a pixel and the reset voltage are sampled 1000 times each leading to image readout times of about 25 s. Typical noise levels are 3-6 electrons (RMS).

In Fig. 4 a fit of the cluster-integrated ADC distribution to a sum of two Gaussians is shown. The relative position of the higher peak w.r.t. the main peak is fixed in the fit to the nominal 6.5 keV/5.9 keV value of the two main X-ray lines from Mn_β and Mn_α. The amplitudes and widths are fitted parameters. For the 5.9 keV peak, the resulting width is 1.9% rms of the peak value. The number of pixels integrated in each cluster varies but, for a typical 9-pixel cluster, the expected width with 6-electron noise is 1.2%. The contribution from the Fano factor

(0.1 for silicon) carrier statistics is 0.8% for a total expected width of 1.4%.

The attenuation length for 5.9 keV X-rays in silicon is 28 μm.[10] With a detector thickness of 200 μm, most of the energy depositions happen near the CCD back-window. Holes thus drift for 140-200 μm until they reach the buried p-channel, undergoing scattering in the process.

Figure 5 shows the charge-weighted position RMS spread in the 5-μm direction for a collection of X-rays. An average 4.5 μm spread is measured. The expected RMS spread in the transverse direction to the charge drift (for the range of voltages/fields used) is approximately given by[11]

$$\sigma_{diff} = \sqrt{2\left(\frac{kT}{q}\right)\frac{d^2}{\Delta V}}, \qquad (1)$$

where k is the Boltzmann constant, T (153 K) is the temperature, ΔV (~112 V) is the voltage difference between the back-window contact and the buried p-channel, and d (200 μm) is the CCD thickness. This results in an expected 3.1 μm spread. The average size of the primary ionization clouds from 5.9 keV electrons is less than 1 μm[12] and does not add to the expected spread significantly.

B. Soft X-ray characterization at ALS beamline 8.0.1

Beam line 8.0.1 at the Advanced Light Source (ALS) at LBNL is equipped with a RIXS spectrometer with a 1.2 m arm length. The system utilizes a spherical mirror to focus the scattered X-rays from a sample onto a grating where it is dispersed according to energy. The camera dewar was attached to the end of the spectrometer arm with the 6-in. flange. After reaching a vacuum pressure of 1×10^{-8} Torr, the camera was cooled to the −120 °C operating temperature.

In CCD images with sparse ~280 eV (C_K) X-ray illumination regions, single-X-ray clusters were identified with a maxima-finding algorithm with a threshold. The charge of the cluster is obtained from the sum of the maximum pixel and the two adjacent pixels from the neighbor columns (in the 5 μm pitch direction). A shape parameter is calculated from the ratio of the maximum pixel divided by the cluster charge. The top panel of Fig. 6 shows a histogram of the measured
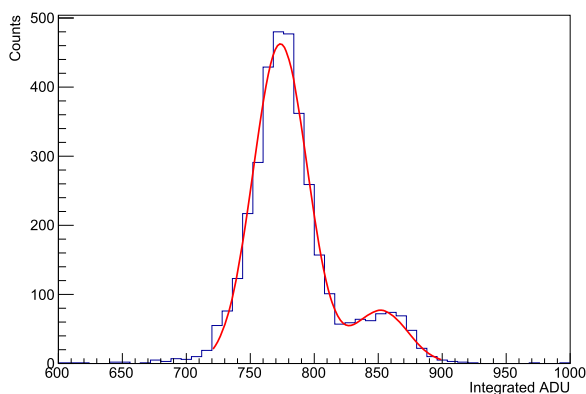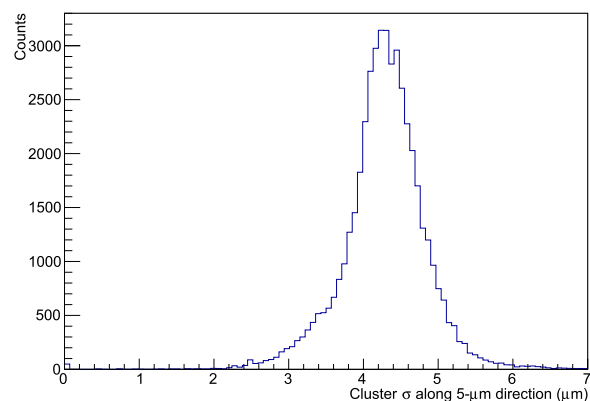

FIG. 4. Raw spectrum from an Iron-55 source. The region near the peaks corresponding to the 5.9 keV and 6.5 keV X-rays is shown. The line is the result of a fit to the sum of two Gaussians with the relative positions of the two peaks fixed to the nominal value while the widths and amplitudes are allowed to vary.

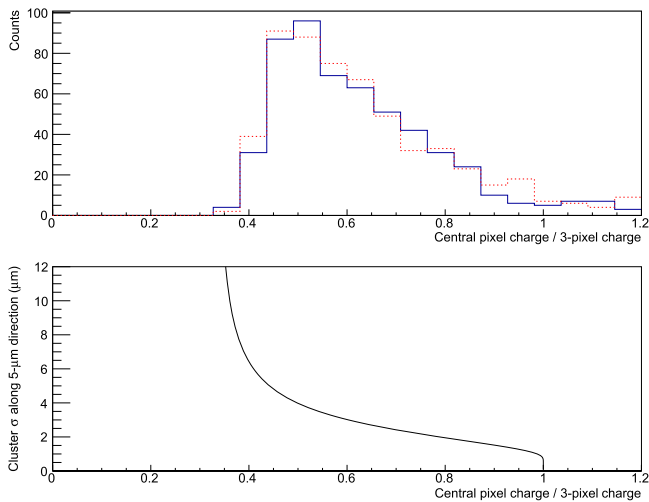FIG. 5. RMS spread of the charge distribution for Iron-55 X-rays in the 5-μm pixel direction.

FIG. 6. Distribution of the shape parameter for isolated ∼280 eV X-rays clusters (solid line, top panel). For a Gaussian PSF the bottom panel shows the (noiseless) calculated PSF as a function of the shape parameter. The dotted histogram in the top panel corresponds to a simulation including clusters with a 4.0 μm PSF superimposed on real image noise.

shape parameter. The lower panel shows the correspondence between the calculated shape parameter and a Gaussian point spread function (PSF) for the collected charge. A simulation built from randomly located 1D-Gaussian clusters (with amplitudes corresponding to C_K X-rays) superimposed on an X-ray-free region of the real image (to accurately reproduce the noise) was used to determine the PSF that best describes the observations. We calculate a χ^2 from the difference between the simulated and measured distributions and obtain a $\sigma = 4.0$ μm $\pm$ 0.2 μm. The dotted histogram in the top panel of Fig. 6 shows the result of that simulation for the best-fit value.

With an X-ray beam energy of ∼280 eV impinging on a graphite sample, initial alignment and focus was achieved by means of CCD images of the bright elastic peak at the 0th-order (mirror-like reflection) diffraction. A small angle (<1°) rotation between the orientation of the CCD columns and the horizontal plane of the spectrometer was apparent and the effect was thereafter removed by a corresponding image rotation in software.

Then, with the spectrometer set to image the 1st-order diffraction, the RMS width of the intrinsically sharp elastic peak was measured to be 10.5 μm, or a little more than 2 pixels. This width was optics-limited and not a measure of the ultimate CCD imager resolution.

Exposure durations of a few seconds or more show a clear indication of cosmic ray tracks. These typically span O(60) pixels in a linear pattern spanning tens of columns and 3-4 rows. This is expected since most cosmic ray muons traverse the 200 μm CCD thickness leaving free holes over the entire trajectory, which get collected in the elongated pixels. Cosmic ray traces are removed from the images, in software, with a simple procedure that replaces the brightest n pixels of every 620-pixel-long column with the median pixel value in that column, where n is typically 10-30.

Figure 7 shows a 40-min-exposure image of ∼280 eV X-rays on a graphite sample with the spectrometer imaging the
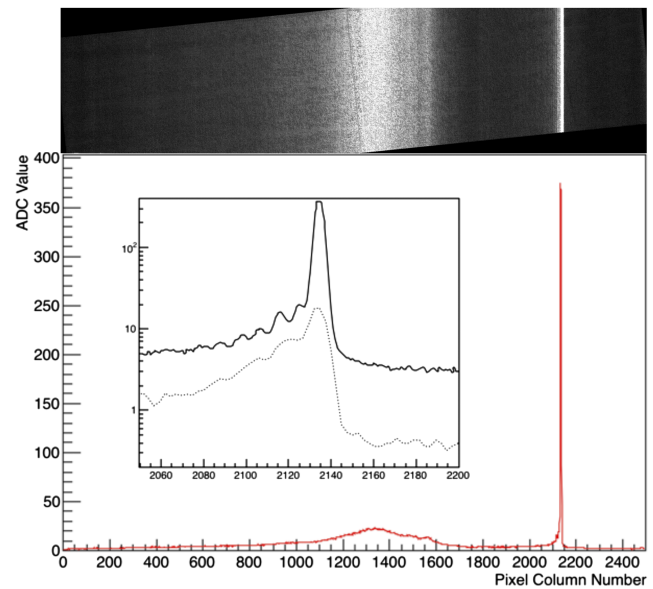

FIG. 7. CCD image of the RIXS spectrum of a graphite sample illuminated with ∼280 eV C_k X-rays (top panel). The image captures the first order diffraction from the grating. Pixels are shown here with square proportions while in reality are elongated 9-fold vertically. The projected spectrum (bottom panel) shows the bright elastic peak and the broad inelastic features. The solid line in the inset shows the details of the spectrum near the elastic peak with clear evidence of an oscillatory pattern for energies below the peak. For comparison, the dotted line is the same spectrum taken with the existing 13.5 × 13.5 μm pixel camera in that spectrometer.

1st-order diffraction. The top panel shows the fully processed CCD image (with: background-image subtraction, quadrant equalization, column interleaving, cosmic-rays removal, and rotation). The bright line on the right is the elastic peak, while the broader features towards the center of the image are due to inelastic scatters. The bottom panel shows the projection (as an average of the value on the pixels along a column after rotation) of the 2D image to produce a 1D spectrum. The inset in the lower panel shows the zoomed-in elastic peak region of the spectrum. An oscillatory feature is clearly visible below the elastic peak with 5-6 smaller equidistant peaks. Peaks in the oscillatory region are about 10 pixels or 50 μm apart.

For comparison, the inset in Fig. 7 shows also the spectrum for the same sample taken with the commercial 13.5 × 13.5-μm-pixel camera currently used in the RIXS spectrometer.

Comparing the positions in the CCD images of the 1th-order diffraction elastic peak for two different X-ray beam energies about 6 eV apart, we obtain the energy-position correspondence: as 0.019 eV per 5 μm-pixel. Thus, these oscillation peaks discernable with our new CCD are approximately 0.19 eV apart.

From a Gaussian fit to the first-order-diffraction elastic peak, we obtain an overall energy resolution of the experimental setup of 90 meV FWHM. This resolution is optics limited and not set by the camera/CCD resolution.

C. Quantum efficiency

A dedicated measurement of the CCD quantum efficiency as a function of energy was performed at the ALS 6.3.2

metrology beam line. The beam illuminates the center of the CCD with a spot of about 0.5 mm diameter. The typical beam power is 200 nW. The CCD camera was cooled to the usual −120 °C. For the measurement, the CCD is not operated in the usual fashion, rather it is operated as a single large diode. All gate and output transistor voltages are set to ground potential, the back-side window contact is set to the usual +100 V and the DC current is measured with a picoampere-sensitive source meter at 0 V connected to the drains of the four reset transistors. This way, a conductive path is made from the buried p-channel in the CCD imaging area, all the way through the source meter.

The metrology beam line is equipped with retractable NIST-calibrated silicon photodiodes that provide absolute photon flux measurements. With the photon flux and the current measurement, a quantum efficiency is then obtained. The energy of the beam was scanned from 100 eV to 1 keV with small gaps near 220 eV and 850 eV where beamline performance limits the accuracy of the measurements. The responsivity of the reference photodiode was calibrated at NIST in the range of 5 nm < λ < 35 nm and extrapolated beyond that.

Figure 8 shows the quantum efficiency of the CCD versus energy in the soft X-ray regime that result from these measurements; it is larger than 75% in the 200 eV-1 keV region.

D. Excess charge and electron accumulation

After O(100) images are taken with the CCD, a noise pattern appears that persists and worsens in subsequent images. The pattern emerges simultaneously in adjacent pairs of columns as an excess of charge in all pixels of the affected columns. For a given column, the effect initially increases with subsequent images but soon reaches a maximum excess charge value. Although the randomly affected columns remain sensitive to charge in their pixels, the shot noise is significantly increased for them.

To erase the effect, the CCD has to be flooded with holes either by setting the substrate and all gate voltages to zero or by raising the reset voltage until holes can flow into the p-channel.

This procedure, while successfully clearing the excess columns, leaves the CCD in a state of high leakage current that requires a 15-20-min wait to return to the normal state of insignificant leakage current.
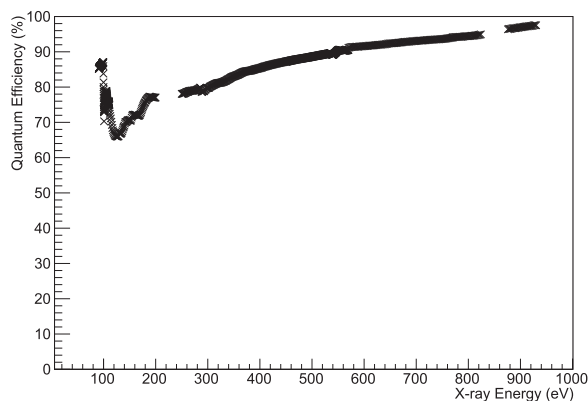
The problem is understood to be due to electrons trapped between columns in the volume between the buried p-channel and the gates' oxide. Dedicated electrostatic simulations of the CCD confirmed that the electric field in that volume indeed acts as an electron trap. As the CCD is clocked for vertical charge transfer, the trapped electrons produce impact ionization that injects holes into the pixels, observed as excess charge, and injects more electrons in the trap.

This issue is unique to this CCD because of the absence of channel stops that would otherwise provide a path out for electrons.

To remedy this, a new version of the CCD is currently being manufactured that enables a mechanism to clock out between-columns electrons and drain them to the substrate.

V. CONCLUSIONS AND FUTURE DEVELOPMENTS

We have developed a new 5 μm-pitch CCD that provides excellent position resolution with an intrinsic point spread function of 4.0 μm for X-rays from 200 eV and up. This position resolution, along with the large dynamic range of the sensor, enables the observation of narrow spectral features in individual RIXS images regardless of whether they appear in the bright or dim regions of the spectrum. Therefore, this new sensor improves the information content without increasing the data volume or the system complexity.

While designed to make use of intrinsic resolution, for low occupancy images, this CCD can also be used in centroiding mode if the exposures are short enough to produce non-overlapping X-ray clusters. In this mode, the calculated centroid position resolution is <2 μm for all X-ray energies above 200 eV as shown in Fig. 9.

The device operating parameters were defined using X-rays from ^{55}Fe sources. Measurements with the RIXS spectrometer at the ALS 8.0.1 beam line demonstrated the improved performance and potential of the new camera, showing spectral features in a graphite sample that previously could not be resolved. A dedicated measurement of the quantum efficiency of the CCD at the ALS 6.3.2 metrology beam line yielded more than 75% efficiency in the 200 eV-1 keV region.
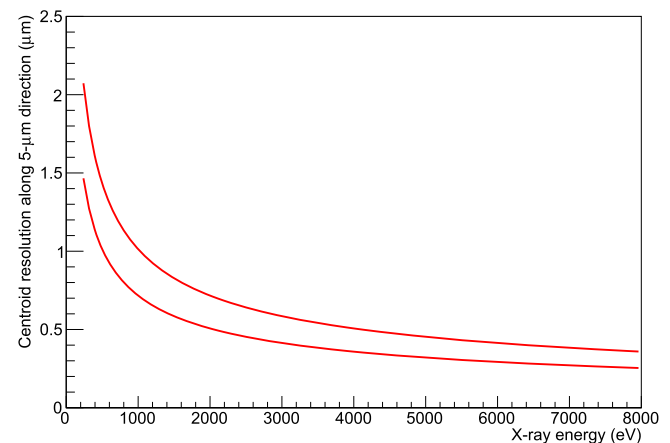
FIG. 8. Quantum efficiency of the CCD as measured in the ALS 6.3.2 metrology beam line.

FIG. 9. Expected centroid position resolution, given the 4.0 μm measured charge spread for 3 *e* (lower line) and 6 *e* (higher line) noise levels.

A new version of the CCD is currently being manufactured with ×4 larger area. The new device will have a slightly modified architecture to enable the clocking out and removal of electrons accumulated between columns that produce, in the current device, column excess charge after extended operation.

For the new version of the device, we plan to replace the ISDP back window with a molecular beam epitaxy (MBE) process that can make thinner depositions through a lower temperature process. With this process, no re-metallization will be needed, thus drastically simplifying the manufacturing of devices as well as allowing devices thinner than 200 μm to further improve the position resolution.

ACKNOWLEDGMENTS

[1]L. J. P. Ament, M. van Veenendaal, T. P. Devereaux, J. P. Hill, and J. van den Brink, Rev. Mod. Phys. **83**(2), 705 (2011).

[2]See www.andor.com for Andor Technology Ltd., 7 Millennium Way, Springvale Business Park, Belfast BT12 7AL, United Kingdom.

[3]See xcam.co.uk for XCAM LIMITED, 2 Stone Circle Road, Round Spinney Industrial Estate, Northampton, NN3 8RF, United Kingdom.

[4]M. R. Soman *et al.*, Nucl. Instrum. Methods Phys. Res., Sect. A **731**, 47 (2013).

[5]M. R. Soman *et al.*, J. Instrum. **8**, C01046 (2013).

[6]S. E. Holland, D. E. Groom, N. P. Palaio, R. J. Stover, and M. Wei, IEEE Trans. Electron Devices **50**, 225 (2003).

[7]D. Doering, Y.-D. Chuang, N. Andresen, K. Chow, D. Contarato, C. Cummings, E. Domning, J. Joseph, J. S. Pepper, B. Smith, G. Zizka, C. Ford, W. S. Lee, M. Weaver, L. Patthey, J. Weizeorick, Z. Hussain, and P. Denes, Rev. Sci. Instrum. **82**, 073303 (2011).

[8]R. J. Hanisch, A. Farris, E. W. Greisen, W. D. Pence, B. M. Schlesinger, P. J. Teuben, R. W. Thompson, and A. Warnock, Astron. Astrophys. **376**, 359 (2001).

[9]C. A. Schneider, W. S. Rasband, and K. W. Eliceiri, Nat. Methods **9**(7), 671 (2012).

[10]B. L. Henke, E. M. Gullikson, and J. C. Davis, At. Data Nucl. Data Tables **54**(2), 181 (1993).

[11]S. E. Holland, N. W. Wang, and W. W. Moses, IEEE Trans. Nucl. Sci. **44**, 443 (1997).

[12]J. C. Ashley, C. J. Tung, R. H. Ritchie, and V. E. Anderson, IEEE Trans. Nucl. Sci. **23**, 1833 (1976).